# A multiscale continuous Galerkin method for stochastic simulation and robust design of wave propagation through heterogeneous materials

F. Vidal-Codina[a,1,*], J. Saà-Seoane[a,1], N. C. Nguyen[a,1], J. Peraire[a,1]

[a]*Department of Aeronautics and Astronautics, Massachusetts Institute of Technology, Cambridge, MA 02139, USA*

arXiv:1610.00625v1 [math.NA] 3 Oct 2016

**Abstract**

We present a multiscale continuous Galerkin (MSCG) method for the fast and accurate simulation of time-harmonic wave propagation problems through heterogeneous media. This method exploits lattice structures to reduce the size of the global linear system by orders of magnitude. Next, we extend the MSCG method to stochastic simulation and optimization problems by augmenting the method with the following ingredients: (1) a reference domain formulation that allows us to treat geometric errors and manufacturing uncertainties in a consistent manner; (2) a reduced basis approximation at the subdomain level that drastically accelerates the solution of the parametrized local subproblems; (3) computation of a gradient of an objective function; and (4) a model and variance reduction technique that enables the accelerated computation of statistical outputs by exploiting the statistical correlation between the MSCG method and the reduced basis approximation. The proposed method is thus well suited for both deterministic and stochastic simulations, as well as robust design of heterogeneous materials. We provide numerical results to demonstrate the convergence of the MSCG method, as well as two photonic crystal applications to illustrate its advantages for stochastic simulation and robust design problems.

*Keywords:* Wave propagation, photonics, multiscale methods, continuous Galerkin, model reduction, variance reduction, multilevel Monte Carlo method, stochastic simulation, robust design

## 1. Introduction

A field that has attracted significant interest in recent years is the study of wave propagation through heterogeneous materials such as photonic crystals, which are engineered to exhibit properties that cannot be found in homogeneous materials. Photonic crystals are assembled by combining conventional materials in lattice structures usually at the microscopic level. Their interaction with acoustic and electromagnetic waves produces several wave phenomena that are not attainable with ordinary materials. A highly interesting phenomenon is the photonic bandgap, a broad range of frequencies for which light waves are disallowed to propagate through a periodic optical nanostructure [52]. These structures enable us to control the transmission of light by creating defects in the crystal, since the photons traveling at any frequency within the band gap are exponentially attenuated within the crystal, thus allowing to guide light in the defect. Moreover, this effect happens in all directions unlike total internal reflection (TIR). Photonic crystals have applications in fibers [35, 50], waveguides [28, 31] and superlenses [38, 45].

*Corresponding author

*Email addresses:* fvidal@mit.edu (F. Vidal-Codina), jsaa@mit.edu (J. Saà-Seoane), cuongng@mit.edu (N. C. Nguyen), peraire@mit.edu (J. Peraire)

[1]This work was supported by AFOSR Grant No. FA9550-11-1-0141, AFOSR Grant No. FA9550-12-0357, and the Singapore-MIT Alliance.

The simulation of wave propagation phenomena in heterogeneous media has been a very active field of research. One of the most widely used is the finite-difference time domain (FDTD) method [36, 43, 54, 55]. The main drawbacks of the FDTD method, despite being simple and efficient, are the difficulties to treat complex geometries, irregular domains and different length scales. The finite element (FE) method [27, 51, 58] is also very popular for solving wave propagation problems thanks to the ability of handling complex geometries and inhomogeneous materials, as well as perform $h/p$ adaptivity. Furthermore, material interface conditions and boundary conditions can be implemented in a natural manner. Although low order methods are often used due to its simplicity, high order methods [2, 21] are more accurate and efficient for wave propagation problems. Both the FD and FE methods have been used to study the propagation of waves through photonic crystals [19, 37, 48, 53].

The ability to accurately simulate wave propagation in photonic crystals presents some challenges beyond traditional simulation techniques. First, wave phenomena usually involve complex geometries and a mismatch in critical length scales, which can be of several orders of magnitude. Resolving the small scales may require an enormous amount of grid points. Moreover, the mathematical model (e.g., Helmholtz and Maxwell's equations) may not capture the real physical phenomena accurately enough due to simplifications and uncertainty in the model data, such as geometry errors, material properties, and boundary conditions.

Several methods have been developed to deal with multiple scales. The study of problems with multiple scales in composite materials and porous media has received great attention [34]. Homogeneization methods [5] allow the treatment of multiscale features by constructing a coarse-scale models wherein the small scales are accounted. A different class of methods are the multiscale FE method [22, 23] and the mixed multiscale FE method [14], which have been successfully applied to multiscale elliptic problems. The main drawback of these methods is their strong dependence on the boundary conditions of the subproblems and boundary resonances for strong interface heterogeneities. A class of methods that are based on domain decomposition are the mortar element methods [8, 9], where we pursue an independent discretization of each subdomain enabling adaptivity and sliding meshes. The mortar element method allows for a great flexibility in the definition of the subdomains, making them particularly attractive for problems with complex geometries. Other methods include the multiscale DG method [1], which blends the approaches above by using the formulation arising from multiscale FE methods and weak continuity at the interfaces. Other approaches include the hybridized multiscale DG method [40], the geometric multiscale FEM [10], and the method of polarized traces [59] for high-frequency problems.

In this paper, we will present the multiscale continuous Galerkin (MSCG) method to simulate wave propagation problems for structured materials. This method is an extension of the hybridized continuous Galerkin method introduced in [15] and the hybridized multiscale DG method [40]. The multiscale CG method possesses considerable advantages over other simulation methods. First, the multiscale discretization produces a significantly smaller global linear system than that of other numerical methods owing to the multilevel static condensation of degrees of freedom. Second, for a variety of problems it exploits repetitive patterns or structure to rapidly construct the global linear system by solving a small number of subproblems. As a result, the method can provide fast and accurate simulations of acoustic and electromagnetic wave problems on an unprecedented scale, where current numerical methods fail to resolve.

Furthermore, we will also consider the simulation and robust design of wave propagation problems in the presence of fabrication uncertainties and design tolerances. For complicated 2d and 3d structures the interaction of acoustic and electromagnetic waves with heterogeneous materials is in general non-intuitive, and small perturbations in the microscopic structure can lead to significant disparities in the performance of the device. To that end, we augment the MSCG method with the following ingredients: (1) a reference domain formulation [46] that allows us to treat geometric errors and manufacturing uncertainties in a consistent manner; (2) a reduced basis approximation [3, 24, 25, 41, 42, 47, 49] at the subdomain level that drastically accelerates the solution of the parametrized local subproblems; (3) an adjoint technique for computing gradients of an output functional; and (4) a model and variance reduction technique [56, 57] that enables the accelerated computation of statistical outputs by exploiting the statistical correlation between the MSCG method and the reduced basis approximation.

This article is organized as follows. In Section 2, we introduce the wave propagation problem and present the MSCG method. In Section 3, we extend our approach to stochastic simulation and robust design problems. In Section 4, we present numerical results to demonstrate the performance of the proposed method. Finally, we conclude in Section 5 by discussing some directions for future research.

## 2. The multiscale continuous Galerkin method

### *2.1. Problem statement*

The propagation of electric and magnetic fields $\mathbf{E}$, $\mathbf{H}$ is governed by Maxwell's equations. However, under some assumptions, the three-dimensional Maxwell's equations may be reduced to the following scalar Helmholtz equation in a domain $\Omega \in \mathbb{R}^2$ with Lipschitz boundary $\partial\Omega$:

$$-\nabla \cdot (\rho(\mathbf{x})\nabla u) - \kappa^2(\mathbf{x})u = f, \qquad \mathbf{x} \in \Omega\ , \tag{1a}$$

$$\rho\nabla u \cdot \mathbf{n} = h, \qquad \mathbf{x} \in \partial\Omega_N\ , \tag{1b}$$

$$u\ = u_D, \qquad \mathbf{x} \in \partial\Omega_D\ , \tag{1c}$$

The above equation may represent two different polarizations of the electromagnetic wave of frequency $\omega$. In TM (transverse magnetic) or E-polarization we assume the magnetic field is confined to the plane of propagation (which we assume the $x-y$ plane), that is $\mathbf{H} = (H_x, H_y, 0)$, and that the electric field is perpendicular to this plane $\mathbf{E} = (0, 0, E_z)$. Conversely, in TE (transverse electric) or H-polarization the electric field is confined to the plane and the magnetic field is perpendicular to it, that is $\mathbf{E} = (E_x, E_y, 0)$ and $\mathbf{H} = (0, 0, H_z)$. The parameters in (1) are $\rho = 1$, $\kappa^2 = \omega^2\varepsilon(x)$ and $u = E_z$ for TM waves, and for TE waves $\rho = \varepsilon(\mathbf{x})^{-1}$, $\kappa^2 = \omega^2$ and $u = H_z$. The flow of electromagnetic power is governed by the time average of the Poynting vector, which can be expressed as $\mathbf{S} = \rho/(2\omega)\Re\left[iu\nabla u^\dagger\right]$, where $^\dagger$ denotes the conjugate transpose.

The Helmholtz equation above assumes a finite domain. Nonetheless, wave propagation problems often occur in unbounded domains. In order to numerically simulate such phenomena, we use the Perfectly Matched Layers (PMLs) [6] by transforming the differential operators to include imaginary values through

$$\frac{\partial}{\partial x} \to \frac{1}{1 - \frac{i\sigma(x)}{\omega}} \frac{\partial}{\partial x}, \tag{2}$$

where $\sigma > 0$ turns the oscillating solution into an exponentially decaying one in the $x$-direction, whereas $\sigma = 0$ leaves the Helmholtz equation unchanged. We refer to [29] for a detailed discussion of the PMLs.

### *2.2. Reference domain formulation*

Let us assume that the physical domain $\Omega$ depends on and thus varies with some geometry parameters $\boldsymbol{z}$ on a compact set. We want to solve the problem (1) for many different realizations of $\boldsymbol{z}$. In such scenario, it is much more convenient to map the physical domain $\Omega$ onto a fixed reference domain $\Omega_{\mathbf{r}}$. Following Persson *et al.* [46], we assume a one-to-one mapping given by a diffeomorphism $\mathfrak{G}$ from the reference domain $\Omega_{\mathbf{r}} \in \mathbb{R}^n$ with coordinates $\mathbf{X}$ to the physical domain $\Omega \in \mathbb{R}^n$ with coordinates $\mathbf{x}$. The mapping can be expressed as $\mathbf{x} = \mathfrak{G}(\mathbf{X}, \boldsymbol{z})$, where $\boldsymbol{z}$ parametrizes the mapping. The mapping deformation gradient and its Jacobian are defined $\mathcal{G} = \nabla_{\mathbf{r}}\mathfrak{G}$ and $g = \det\mathcal{G}$, respectively. Note that $\nabla = \mathcal{G}^{-T}\nabla_{\mathbf{r}}$.

To obtain the transformed equation on the reference space we integrate on a volume and use the divergence theorem. In particular, the transformed equation on the reference domain reads

$$\begin{aligned}\int_v \left[\nabla \cdot \rho\nabla u + \kappa^2 u - f\right] dv &= \int_s \rho\nabla u \cdot \mathbf{n} ds + \int_v (\kappa^2 u - f) dv = \int_S g\mathcal{G}^{-1}\rho\nabla u \cdot \mathbf{N} dS + \int_V (\kappa^2 u - f) g dV \\ &= \int_V \left[\nabla_{\mathbf{r}} \cdot g\mathcal{G}^{-1}\rho\nabla u + \kappa^2 g u - fg\right] dV = \int_V \left[\nabla_{\mathbf{r}} \cdot \rho g\mathcal{G}^{-1}\mathcal{G}^{-T}\nabla_{\mathbf{r}} u + \kappa^2 g u - fg\right] dV\end{aligned} \tag{3}$$

where we recall the following relations $dv = g dV$ and $\mathbf{n} ds = g \mathcal{G}^{-1} \mathbf{N} dS$. If we transform the boundary conditions as well we arrive to

$$-\nabla_{\mathbf{r}} \cdot (\rho \boldsymbol{G} \nabla_{\mathbf{r}} u) - \kappa^2 u\, g = f\, g, \qquad \mathbf{x} \in \Omega_{\mathbf{r}} \,, \tag{4a}$$

$$\rho \nabla_{\mathbf{r}} u \cdot \mathbf{n} = h\, g_s, \qquad \mathbf{x} \in \partial\Omega_{\mathbf{r},N} \,, \tag{4b}$$

$$u \;= u_D, \qquad \mathbf{x} \in \partial\Omega_{\mathbf{r},D} \,, \tag{4c}$$

where $\boldsymbol{G} = g \mathcal{G}^{-1} \mathcal{G}^{-T}$ and $g_s$ is the restriction of the jacobian $g$ to the face.

### *2.3. Heterogeneous materials*

As mentioned earlier, our goal in this paper is to develop a method for efficiently simulating wave propagation through heterogeneous materials. As a motivating example, we consider a waveguide in Figure 1 (left) consisting of dielectric rods in air. Our work relies on solving for a small number of subproblems, in this case only the subdomain with the rod and the defect subdomain (no rod), thus exploiting the repeated patterns. Unfortunately, in real photonic applications, all of these rods are different mainly due to fabrication tolerances and manufacturing errors that arise as a consequence of the extreme-scale fabrication techniques, see Figure 1 (right). Thus, in order to achieve truly predictive simulations one must take into account these variations. For simplicity of exposition, we consider circular rods as an example. The extension to multiple types/shapes of rods is straightforward.

In this case, the reference domain $\Omega_{\mathbf{r}}$ refers to the structure with perfectly circular rods, whereas the physical domain $\Omega$ is used to describe the real structure with varying rods. We assume that both domains may be split using $M$ non-overlapping subdomains such that $\overline{\Omega} = \bigcup_{m=1}^{M} \overline{\Omega}^m$, $\overline{\Omega}_{\mathbf{r}} = \bigcup_{m=1}^{M} \overline{\Omega}_{\mathbf{r}}^m$. Thus, instead of solving (1) on $\Omega$, we solve (4) on $\Omega_{\mathbf{r}}$. Furthermore, we shall assume the one-to-one diffeomorphism deforms each subdomain independently leaving the subdomain interfaces fixed, hence for $M$ subdomains the mapping is defined as $\mathfrak{G} = \mathfrak{G}^1 \times \ldots \times \mathfrak{G}^M$. If we then set $\boldsymbol{z} \coloneqq \boldsymbol{z}^1 \times \ldots \times \boldsymbol{z}^M$, the $m$-th subdomain transforms as $\Omega^m = \mathfrak{G}^m(\Omega_{\mathbf{r}}^m, \boldsymbol{z}^m)$, and we abuse the notation by referring to the mapping and its differential quantities as $\mathfrak{G}^m, g^m, \mathcal{G}^m, \boldsymbol{G}^m$.

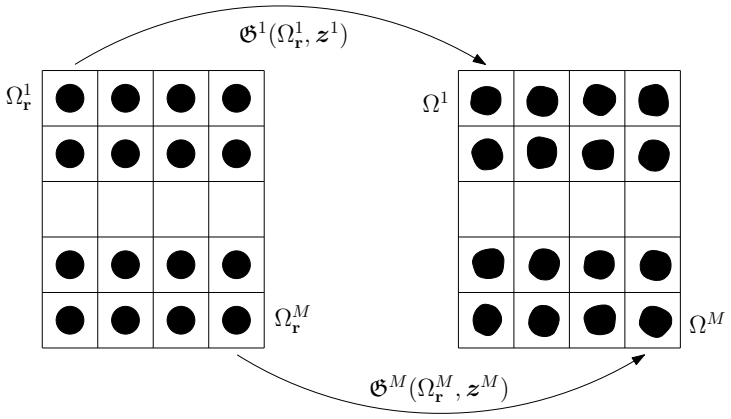


Figure 1: Reference domain (left), physical domain (right) and subdomain mapping.

### *2.4. MSCG method*

Let us introduce the MSCG method to solve the governing equation on the fixed reference domain. We first define a triangulation $\mathcal{T}_h^m$ on each subdomain $\Omega_{\mathbf{r}}^m$. The triangulation of the entire reference domain

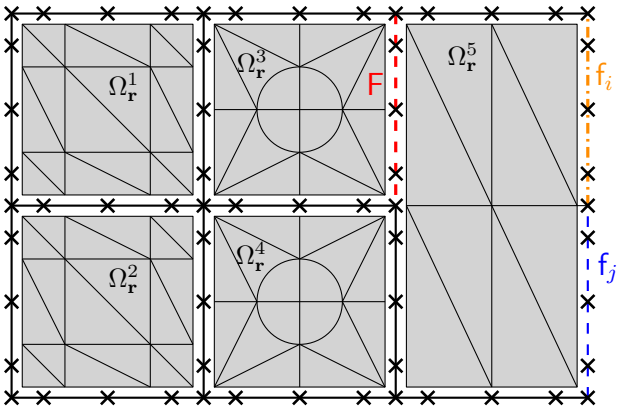


(a) Local subdomains and global unknowns. Interfaces discretized with one 4-th order element except the right boundary, where two elements $\mathsf{f}_i$, $\mathsf{f}_j$ of order 4 are used.

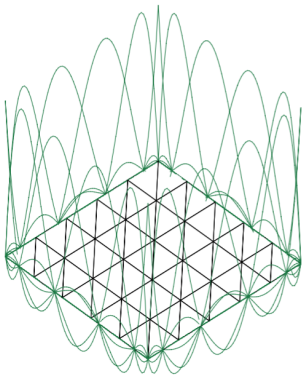

(b) Basis of Lagrange polynomial at subdomain boundary, using one element of order 5 per interface.

Figure 2: Multiscale schematics for local problems and Lagrange polynomial at interfaces.

is thus $\mathcal{T}_h = \bigcup_{m=1}^{M} \mathcal{T}_h^m$. In Figure 2a we show the division of a reference domain in 5 subdomains with its corresponding triangulations.

Let $\mathsf{F}$ be a subdomain face that coincides with either $\partial\Omega_{\mathbf{r}}^m \cap \partial\Omega_{\mathbf{r}}^n$ $(n \neq m)$ or $\partial\Omega_{\mathbf{r}}^m \cap \partial\Omega_{\mathbf{r}}$. The collection of subdomain faces of $\mathcal{T}_h$ is $\{\mathsf{F}^\ell\}_{\ell=1}^{L}$. For each subdomain face $\mathsf{F}^\ell$, we subdivide it into $N^\ell$ elements $\mathsf{f}_i^\ell$, $1 \leq i \leq N^\ell$. Thus we define the set of face elements as $\mathcal{F}_\mathsf{f} = \{\mathsf{f}_i^\ell,\, 1 \leq i \leq N^\ell, 1 \leq \ell \leq L\}$. For instance, in Figure 2a, the subdomain faces coincide with the face elements except for the rightmost boundary, wherein the face is subdivided into two elements $f_i$ (dashed dotted) and $f_j$ (dash).

We can now introduce our approximation spaces as

$$W_h = \{w \in L^2(\Omega_{\mathbf{r}}) : w \in \mathcal{C}^0(\Omega_{\mathbf{r}}^m),\, w|_T \in \mathcal{P}^{p^m}(T), \forall T \in \mathcal{T}_h^m,\, 1 \leq m \leq M\}, \tag{5a}$$

$$M_h = \{\mu \in L^2(\partial\Omega_{\mathbf{r}}^m \,:\, \Omega_{\mathbf{r}}^m \in \mathcal{T}_h) : \mu|_{\partial\Omega_{\mathbf{r}}^m} = w|_{\partial\Omega_{\mathbf{r}}^m},\ \text{for } w \in W_h\}, \tag{5b}$$

$$V_h = \{v \in \mathcal{C}^0(\mathcal{F}_\mathsf{f}) : v|_\mathsf{f} \in \mathcal{P}^{p^\mathsf{f}}(\mathsf{f}), \forall \mathsf{f} \in \mathcal{F}_\mathsf{f}\}, \tag{5c}$$

where $\mathcal{P}^{p^m}(T)$ is the space of polynomials of degree at most $p^m$ on $T \in \mathcal{T}_h^m$ and $\mathcal{P}^{p^\mathsf{f}}(\mathsf{f})$ is the space of polynomials of degree at most $p^\mathsf{f}$ on $\mathsf{f} \in \mathcal{F}_\mathsf{f}$. Note that we allow variation of polynomial degrees on subdomains. To impose the Dirichlet boundary condition, we introduce $V_h(u_D) = \{v \in V_h : v = \mathsf{P}^{V_h}(u_D),\ \text{on } \partial\Omega_{\mathbf{r},D}\}$, where the operator $\mathsf{P}^{V_h}$ represents the $L^2$ projection onto the space $V_h$ for the boundary $\partial\Omega_{\mathbf{r},D}$.

We then introduce the auxiliary variable $q_h$ which approximates of the normal component of the flux $q = \rho \boldsymbol{G} \nabla_{\mathbf{r}} u \cdot \mathbf{N}$. We then seek an approximation $(u_h, \lambda_h, q_h) \in W_h \times V_h(u_D) \times M_h$ such that

$$(\rho \boldsymbol{G} \nabla_{\mathbf{r}} u_h, \nabla_{\mathbf{r}} w)_{\Omega_{\mathbf{r}}} - (g\,\kappa^2 u_h, w)_{\Omega_{\mathbf{r}}} - \sum_{m=1}^{M} \langle q_h, w \rangle_{\partial\Omega_{\mathbf{r}}^m} = (g\,f, w)_{\Omega_{\mathbf{r}}}, \tag{6a}$$

$$u_h = \mathsf{P}^{W_h}(\lambda_h), \qquad \text{on } \mathcal{F}_\mathsf{f} \tag{6b}$$

$$\sum_{m=1}^{M} \langle q_h, v \rangle_{\partial\Omega_{\mathbf{r}}^m} = \langle g_s\, h, v \rangle_{\partial\Omega_{\mathbf{r},N}}, \tag{6c}$$

for all $(w, v) \in W_h \times V_h(0)$, where the operator $\mathsf{P}^{W_h}$ represents the projection onto the space $W_h$. Note that equation (6c) enforces continuity of the normal component of the flux across interfaces of the subdomains.

We next eliminate the equations and unknowns of $(u_h, q_h)$ using Schur complement to obtain a formulation in terms of $\lambda_h$ only. This can be achieved by considering two subproblems for each subdomain $\Omega_{\mathbf{r}}^m$: the first subproblem maps the function $f \in L^2(\Omega)$ to $u_h^f|_{\Omega_{\mathbf{r}}^m} \in W_h^m(0)$ defined in (7a), and the second subproblem maps $\eta \in V_h$ to $u_h^\eta|_{\Omega_{\mathbf{r}}^m} \in W_h^m(\eta)$ defined in (7b) as follows

$$(\rho \boldsymbol{G}^m \nabla_{\mathbf{r}} u_h^f, \nabla_{\mathbf{r}} w)_{\Omega_{\mathbf{r}}^m} - (g^m\, \kappa^2 u_h^f, w)_{\Omega_{\mathbf{r}}^m} = (g^m\, f, w)_{\Omega_{\mathbf{r}}^m}, \quad \forall w \in W_h^m(0), \tag{7a}$$

$$(\rho \boldsymbol{G}^m \nabla_{\mathbf{r}} u_h^\eta, \nabla_{\mathbf{r}} w)_{\Omega_{\mathbf{r}}^m} - (g^m\, \kappa^2 u_h^\eta, w)_{\Omega_{\mathbf{r}}^m} = 0, \qquad \forall w \in W_h^m(0). \tag{7b}$$

Here $W_h^m = \{w \in \mathcal{C}^0(\Omega_{\mathbf{r}}^m),\, w|_T \in \mathcal{P}^{p^m}(T), \forall T \in \mathcal{T}_h^m\}$ and $W_h^m(\eta) = \{w \in W_h^m : w = \mathtt{P}^{W_h^m}(\eta),\ \text{on } \partial\Omega_{\mathbf{r}}^m\}$, where the operator $\mathtt{P}^{W_h^m}$ represents the projection onto the space $W_h^m$. Finally, we find the Lagrange multiplier $\lambda_h \in V_h(u_D)$ as a unique solution of the weak formulation

$$(\rho \boldsymbol{G} \nabla_{\mathbf{r}} u_h^{\lambda_h}, \nabla_{\mathbf{r}} u_h^v)_{\Omega_{\mathbf{r}}} - (g\, \kappa^2 u_h^{\lambda_h}, u_h^v)_{\Omega_{\mathbf{r}}} = (g\, f, u_h^v)_{\Omega_{\mathbf{r}}} + \langle g_s\, h, v\rangle_{\Omega_{\mathbf{r},N}} \tag{8}$$

for $v \in V_h(0)$, and compute the numerical solution $u_h = u_h^f + u_h^{\lambda_h}$.

The main feature of MSCG is the flexibility of mesh generation and $h/p$ adaptivity at the subdomain level, since the local subproblem on a subdomain is independent of the remaining subdomains, as it only depends on the interfaces. Hence, the local subproblem information may be statically condensed at the interfaces. The idea is to relax the continuity restriction at the subdomain interface and impose it back through a set of Lagrange multipliers $\lambda$, which correspond to the unique solution of the variational formulation on the skeleton. Once the global solution is obtained, the solution for the local subproblems can be recovered independently for each subdomain. Another important advantage of the MSCG is that the solution at the interfaces can be approximated with a different polynomial space than that of the subproblems, for instance using Lagrange interpolation polynomials of higher order at Chebyshev nodes, thus drastically reducing the size of the global system that needs to be solved. Finally, continuity of the approximate solution across subdomains is enforced by imposing Dirichlet boundary conditions for each subdomain that coincide with the value of the global solution at the interfaces.

### *2.4.1. MSCG implementation*

We describe how to implement the MSCG method. Firstly, let us assume the total number of global and local degrees of freedom in the problem is given by $\mathcal{N}_g$, $\mathcal{N}_\ell$ respectively, and that the superscript $m$ identifies the global/local degrees of freedom for a specific subdomain. Let $V_h$ be spanned by a set of global basis functions $\{\varphi_i\}_{i=1}^{\mathcal{N}_g}$. These basis functions are Lagrange polynomials interpolating on the Chebyshev nodes as shown in Figure 2b. Then we have $\lambda_h = \sum_{i=1}^{\mathcal{N}_g} \Lambda_i \varphi_i(\mathbf{X})$, where $\boldsymbol{\Lambda} = (\Lambda_1, \ldots, \Lambda_{\mathcal{N}_g})$ solves the linear system

$$\mathbb{K}\boldsymbol{\Lambda} = \mathbb{F} \tag{9}$$

where the matrices $\mathbb{K} \in \mathbb{R}^{\mathcal{N}_g \times \mathcal{N}_g}$, $\mathbb{F} \in \mathbb{R}^{\mathcal{N}_g}$ are given by

$$\mathbb{K}_{ij} = (\rho \boldsymbol{G} \nabla_{\mathbf{r}} u_h^{\varphi_j}, \nabla_{\mathbf{r}} u_h^{\varphi_i})_{\Omega_{\mathbf{r}}} - (g\, \kappa^2 u_h^{\varphi_j}, u_h^{\varphi_i})_{\Omega_{\mathbf{r}}}, \qquad 1 \le i, j \le \mathcal{N}_g \tag{10a}$$

$$\mathbb{F}_i = (g\, f, u_h^{\varphi_i})_{\Omega_{\mathbf{r}}} + \langle g_s\, h, \varphi_i\rangle_{\partial\Omega_{\mathbf{r},N}}, \qquad 1 \le i \le \mathcal{N}_g, \tag{10b}$$

Of course, the Dirichlet boundary condition must also be enforced when solving (9) for $\boldsymbol{\Lambda}$. Note that $u_h^{\varphi_i}$ is the solution of the local subproblems (7b) for $\eta = \varphi_i$ and that we need to solve (7b) only on the subdomains for which $\varphi_i$ is non-zero.

In practice, we assemble the linear system (9) by computing the local quantities as follows. Let $\{\varphi_i^m\}_{i=1}^{\mathcal{N}_g^m}$ be a set of local basis functions of the space $V_h$ on the subdomain $\Omega_{\mathbf{r}}^m$. Then the local stiffness matrices and load vectors are computed as

$$\mathbb{K}_{ij}^m = (\rho \boldsymbol{G}^m \nabla_{\mathbf{r}} u_h^{\varphi_j^m}, \nabla_{\mathbf{r}} u_h^{\varphi_i^m})_{\Omega_{\mathbf{r}}^m} - (g^m\, \kappa^2 u_h^{\varphi_j^m}, u_h^{\varphi_i^m})_{\Omega_{\mathbf{r}}^m}, \qquad 1 \le i, j \le \mathcal{N}_g^m, \tag{11a}$$

$$\mathbb{F}_i^m = (g^m\, f, u_h^{\varphi_i^m})_{\Omega_{\mathbf{r}}^m} + \langle g_s^m\, h, \varphi_i^m\rangle_{\partial\Omega_{\mathbf{r},N}^m}, \qquad 1 \le i \le \mathcal{N}_g^m, \tag{11b}$$

where the functions $u_h^{\varphi_i^m} \in W_h^m(\varphi_i^m)$ are obtained by solving

$$(\rho \boldsymbol{G}^m \nabla_{\mathbf{r}} u_h^{\varphi_i^m}, \nabla_{\mathbf{r}} w)_{\Omega_{\mathbf{r}}^m} - (g^m \kappa^2 u_h^{\varphi_i^m}, w)_{\Omega_{\mathbf{r}}^m} = 0, \quad \forall w \in W_h^m(0), \tag{12}$$

for $m = 1, \ldots, M$. The global stiffness matrix $\mathbb{K}$ and load vector $\mathbb{F}$ can now be assembled through the standard finite element assembly procedure. Finally, we recover the numerical solution on any subdomain $\Omega_{\mathbf{r}}^m$ as $u_h|_{\Omega_{\mathbf{r}}^m} = u_h^f|_{\Omega_{\mathbf{r}}^m} + \sum_{i=1}^{\mathcal{N}_g^m} \Lambda_i^m u_h^{\varphi_i^m}$, where $\Lambda_i^m, 1 \leq i \leq \mathcal{N}_g^m$ are the degrees of freedom of $\lambda_h$ on $\Omega_{\mathbf{r}}^m$.

It should be pointed out that if the subdomains belong to the same class then they have the same subproblem. As a result, the number of subproblems is equal to the number of subdomain classes. This feature is one of the key advantages of the MSCG method, which makes it particularly attractive for problems with periodic or repetitive structures.

## 3. Stochastic MSCG

In this section, we introduce an computational approach for computing the statistics of some outputs of interest, such as the transmission power of photonic devices, of stochastic wave propagation problems. The main ingredients of our approach include (1) stochastic modeling to deal with geometry error due to imperfections, (2) reduced basis approximation [3, 42, 47, 49] to reduce the computational cost, (3) variance reduction [20, 39, 56, 57] to accelerate the convergence of the statistical outputs, and (4) adjoint technique to compute the derivatives of the statistical outputs.

### *3.1. Stochastic modeling for geometry error*

In photonic crystals, the most widely used patterns are either dielectric circular rods in air or air holes in a dielectric slab [28]. Ideally, all of these circular rods should have the same radius $R_0$. However, because of technological limitation at micro and nano scales, these circular rods are never perfectly round. In other words, there are a manufacturing tolerance/variability in the circular rods. We will assume that geometry variability is restricted to the radial direction and modeled as function of the angular coordinate $\alpha \in [0, 2\pi]$ with a random field with covariance kernel described in [12]. The geometry error is characterized through the following truncated Karhunen-Loève expansion of the radius:

$$r_0(\boldsymbol{z}) = R_0 + \delta R_0(\boldsymbol{z}) = R_0 \left[ 1 + z_1 \sqrt{\lambda_0/2} + \sum_{d=1}^{D/2} \sqrt{\lambda_d} \left[ z_{2d} \sin\left(d(\alpha + \pi/2)\right) + z_{2d+1} \cos\left(d(\alpha + \pi/2)\right) \right] \right]. \tag{13}$$

Here $\sqrt{\lambda_d} = \sigma \left(\sqrt{\pi} L_c\right)^{1/2} \exp\left(-(d\pi L_c)^2/8\right), d = 0, \ldots, D$, where $\sigma$ is the variance of the covariance kernel and $L_c$ is the correlation length, which is inversely related to the decay of the KL modes. Figure 3b shows some realizations of the rod radius.

We now briefly describe the mapping $\mathfrak{G}^m$ that we use for all rod subdomains. For this work we consider subdomains with both square and triangular symmetry of unit length, discretized with high-order triangulations such that the perimeter of the circle and a bounding box around the origin of length $\ell$ (to avoid the singularity) are well represented, see Figure. The subdomain deforms as $(x, y) = \mathfrak{G}^m(\mathbf{X})$, hence the derivatives $\partial x_i / \partial X_j$ are required for the computations. Using polar coordinates in both spaces and taking into account that modifications are only considered in the radial direction, that is $(r^2, \alpha) = (x^2 + y^2, \arctan y/x)$ and $(R^2, \alpha) = (X^2 + Y^2, \arctan Y/X)$, we can express $x = r(\mathbf{X}) \cos\alpha$ and $y = r(\mathbf{X}) \sin\alpha$. We also note that the boundaries of the domain and bounding box around the origin remain fixed.

In order to define $r(\mathbf{X})$ for the points in the triangulation, we assume that the perimeter of the rod is deformed according to (13), and that the remaining points are linearly deformed according to

$$r(\mathbf{X}) = \begin{cases} B_\ell + (r_0 - B_\ell) \cdot \dfrac{R - B_\ell}{R_0 - B_\ell}, & \text{if } R \leq R_0 \\ r_0 + (B - r_0) \cdot \dfrac{R - R_0}{B - R_0}, & \text{if } R > R_0 \end{cases}. \tag{14}$$

The derivatives $\partial r / \partial x_i$ may be computed with the chain rule. Note there are two distinct types of boundaries, see Figure 3a, and its distance to the origin can described as $B = \sqrt{1 + (Y/X)^2}$ (red) and $B = \sqrt{1 + (X/Y)^2}$ (black). The distance to the boundary of the origin box is similarly computed.

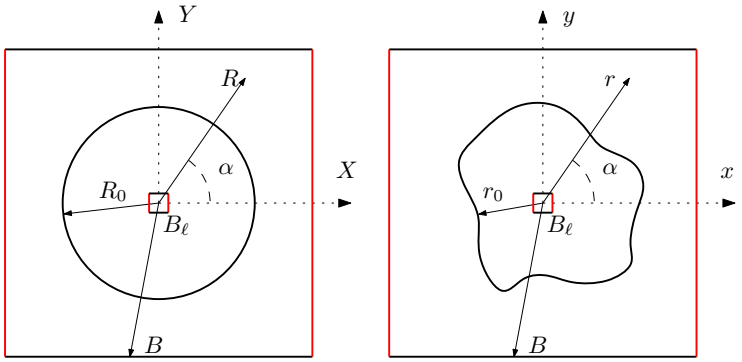


(a) Reference domain (left) and physical domain (right) of square subdomain in polar coordinates.

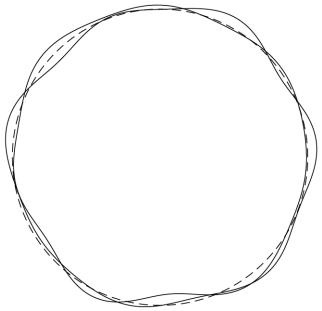

(b) Realizations of radius variation (solid) and reference radius (dashed).

Figure 3: Mapping quantities and sample radius modifications.

### *3.2. Reduced basis approximation*

A key component of our proposed approach is the use of reduced basis approximation to compute approximate solutions at the subdomain level. This will enable us to accelerate the multiscale continuous Galerkin method. We briefly described how a reduced basis is constructed in this framework.

The bilinear forms involved in the local problems (7) depend *nonaffinely* on the parameter vector $\boldsymbol{z}$ since the deformation mapping $\mathfrak{G}$ is nonaffine. To circumvent the nonaffine parameter dependence, we use the discrete empirical interpolation method (DEIM) [11] to approximate, $\boldsymbol{G}(\boldsymbol{X}, \boldsymbol{z})$ and $g(\boldsymbol{X}, \boldsymbol{z})$ with the following affine expansions

$$\boldsymbol{G}_Q(\boldsymbol{X}, \boldsymbol{z}) = \sum_{q=1}^{Q} \sigma_q(\boldsymbol{z}) \overline{\boldsymbol{G}}_q(\boldsymbol{X}), \quad g_K(\boldsymbol{X}, \boldsymbol{z}) = \sum_{k=1}^{K} \varsigma_k(\boldsymbol{z}) \overline{g}_k(\boldsymbol{X}), \tag{15}$$

respectively. For an arbitrary subdomain we now substitute (15) in (7) as an approximation of the geometric properties, and find $u_h^f|_{\Omega_{\mathbf{r}}^m} \in W_h^m(0)$ and $u_h^\eta|_{\Omega_{\mathbf{r}}^m} \in W_h^m(\eta)$ such that

$$\sum_{q=1}^{Q} \sigma_q(\boldsymbol{z}^m)(\rho\, \overline{\boldsymbol{G}}_q^m \nabla_{\mathbf{r}} u_h^f, \nabla_{\mathbf{r}} w)_{\Omega_{\mathbf{r}}^m} - \sum_{k=1}^{K} \varsigma_k(\boldsymbol{z}^m)(\overline{g}_k^m\, \kappa^2 u_h^f, w)_{\Omega_{\mathbf{r}}^m} = \sum_{k=1}^{K} \varsigma_k(\boldsymbol{z}^m)(\overline{g}_k^m\, f, w)_{\Omega_{\mathbf{r}}^m}, \tag{16a}$$

$$\sum_{q=1}^{Q} \sigma_q(\boldsymbol{z}^m)(\rho\, \overline{\boldsymbol{G}}_q^m \nabla_{\mathbf{r}} u_h^\eta, \nabla_{\mathbf{r}} w)_{\Omega_{\mathbf{r}}^m} - \sum_{k=1}^{K} \varsigma_k(\boldsymbol{z}^m)(\overline{g}_k^m\, \kappa^2\, u_h^\eta, w)_{\Omega_{\mathbf{r}}^m} = 0. \tag{16b}$$

for all $w \in W_h^m(0)$.

For subproblem (16b) assume that we are given, for a certain Dirichlet condition $\eta = \varphi_i$, orthonormalized basis functions $\zeta_n^i$, $1 \le n \le N_{\max}$, such that $(\zeta_n^i, \zeta_{n'}^i)_{W_h^m} = \delta_{nn'}$. The associated hierarchical RB space is defined as $W_{i,N}^m = \text{span}\{\zeta_n^i,\, 1 \le n \le N\}$. In our case this spaces are constructed by computing a weighted POD [7] on a set of solutions. The main caveat of this formulation is that we typically have many Dirichlet conditions, which can impact the efficiency of the method since we must solve multiple RB systems. Instead, we propose to develop a single RB space $W_N^m$, where the basis functions $\zeta_n$ are computed with a weighted POD on a set of solutions for all possible Dirichlet boundary conditions. That is, we treat the solutions for the various boundary conditions as independent snapshots, allowing us to assemble and solve only one reduced basis system. For the first subproblem the process is similar if $f$ has spatial dependence, thus the RB needs to be constructed upon all possible variations of the source on the subdomains. Nonetheless, if the source is constant the RB for (16a) may be obtained using the standard RB procedure. The associated RB space that arises from the source problem is $\widetilde{W}_N^m(0)$.

We then apply a Galerkin projection to find a RB solution $\left(u_N^f, u_N^{\varphi_i}\right) \in \widetilde{W}_N^m(0) \times W_N^m(\varphi_i)$ satisfying, for all $(\widetilde{w}, w) \in \widetilde{W}_N^m(0) \times W_N^m(0)$

$$\sum_{q=1}^{Q} \sigma_q(\boldsymbol{z})(\rho\, \overline{\boldsymbol{G}}_q^m \nabla_{\mathbf{r}} u_N^f, \nabla_{\mathbf{r}} \widetilde{w})_{\Omega_{\mathbf{r}}^m} - \sum_{k=1}^{K} \sigma_k(\boldsymbol{z})(\overline{g}_k^m\, \kappa^2 u_N^f, \widetilde{w})_{\Omega_{\mathbf{r}}^m} = \sum_{k=1}^{K} \varsigma_k(\boldsymbol{z})(\overline{g}_k^m\, f, \widetilde{w})_{\Omega_{\mathbf{r}}^m}, \tag{17a}$$

$$\sum_{q=1}^{Q} \sigma_q(\boldsymbol{z})(\rho\, \overline{\boldsymbol{G}}_q^m \nabla_{\mathbf{r}} u_N^{\varphi_i}, \nabla_{\mathbf{r}} w)_{\Omega_{\mathbf{r}}^m} - \sum_{k=1}^{K} \varsigma_k(\boldsymbol{z})(\overline{g}_k^m\, \kappa^2 u_N^{\varphi_i}, w)_{\Omega_{\mathbf{r}}^m} = 0. \tag{17b}$$

The elementary global matrix $\mathbb{K}_{ij}^m$ and vector $\mathbb{F}_i^m$ are then approximated as

$$\mathbb{K}_{ij}^m \approx \sum_{q=1}^{Q} \sigma_q(\boldsymbol{z}^m)(\rho\, \overline{\boldsymbol{G}}_q^m \nabla_{\mathbf{r}} u_N^{\varphi_j}, \nabla_{\mathbf{r}} u_N^{\varphi_i})_{\Omega_{\mathbf{r}}^m} - \sum_{k=1}^{K} \varsigma_k(\boldsymbol{z}^m)(\overline{g}_k^m\, \kappa^2 u_N^{\varphi_j}, u_N^{\varphi_i})_{\Omega_{\mathbf{r}}^m}, \tag{18a}$$

$$\mathbb{F}_i^m \approx \sum_{k=1}^{K} \varsigma_k(\boldsymbol{z}^m)(\overline{g}_k^m f, u_N^{\varphi_i})_{\Omega_{\mathbf{r}}^m} + \sum_{k=1}^{K} \varsigma_k(\boldsymbol{z}^m)\langle \overline{g}_k^m\, h, \varphi_i\rangle_{\partial\Omega_{\mathbf{r},N}^m}. \tag{18b}$$

for $1 \le i, j \le \mathcal{N}_g^m$. The affine parametric dependence enables an Offline-Online computational strategy where the parameter-independent instances are precomputed and stored beforehand, and the cost to obtain the approximate solution $u_N^{\varphi_i}$ for each new parameter value depends only on $Q$, $K$ and $N$.

### *3.3. Model and variance reduction*

Our approach exploits the structure of the problem using the MSCG method and the development of a RB for subdomains under a deformation mapping. We now study how these two different models can be combined to produce fast yet accurate estimates of the statistics of a quantity of interest. We propose a multilevel variance reduction method that exploits the statistical correlation among the different reduced basis approximations and the high-fidelity MSCG discretization to accelerate the convergence rate of the Monte Carlo simulations. The multilevel variance reduction method provides efficient computation of the statistical outputs by shifting most of the computational burden from the high-fidelity MSCG approximation to the reduced basis approximations.

We first introduce a probability space $(\Upsilon, \Sigma, P)$, where $\Upsilon$ is the set of outcomes, $\Sigma$ is the $\sigma$-algebra of the subsets of $\Upsilon$, and $P$ is the probability measure. If $Z$ is a real random variable in $(\Upsilon, \Sigma, P)$ and $\upsilon$ a probability event, we denote its expectation by $E[Z] = \int_\Upsilon Z(\upsilon) dP(\upsilon)$. For an arbitrary subdomain $\Omega_{\mathbf{r}}^m$, we will consider random functions $v$ in $L^2(\Omega_{\mathbf{r}}^m \times \Upsilon)$ equipped with the following norm

$$\|w\|^2 = E\left[\int_{\mathcal{D}} |w(\mathbf{X}, \cdot)|^2 d\mathbf{X}\right] = \int_\Upsilon \int_{\mathcal{D}} |w(\mathbf{X}, \upsilon)|^2 d\mathbf{X}\, dP(\upsilon).$$

We assume that, for a given subdomain $\Omega^m_{\mathbf{r}}$, the parameters that define the geometric mapping $z^m_d(\upsilon)$ for $d = 1\ldots, D$ are mutually independent random variables with zero mean. In addition, we assume that each of the $z^m_d(\upsilon)$ is bounded in the interval $\Gamma^m_d = [-\gamma^m_d, \gamma^m_d]$ with a uniformly bounded probability density function $\pi^m_d : \Gamma^m_d \to \mathbb{R}^+$. It thus follows that, with a slight overloading of notation, we can write $\boldsymbol{z}^m = (z^m_1, \ldots, z^m_D)$ and $\Gamma^m = \prod_{d=1}^D \Gamma^m_d$. Hence, the entire stochastic space is given by $\Gamma = \prod_{m=1}^M \Gamma^m$ and the random variable as $\boldsymbol{z} = \prod_{m=1}^M \boldsymbol{z}^m$.

The solution $u$ of the original problem can be written as a function of $\boldsymbol{z} \in \Gamma$. Now let $s$ be a bounded functional. We introduce a random output $s$ defined as

$$s(\boldsymbol{z}) = s(u(\cdot, \boldsymbol{z})).$$

We are interested in evaluating the expectation and variance of $s$ as

$$E[s] = \int_\Gamma s(\boldsymbol{z}) p(\boldsymbol{z}) d\boldsymbol{z}, \qquad V[s] = \int_\Gamma \left(E[s] - s(\boldsymbol{z})\right)^2 p(\boldsymbol{z}) d\boldsymbol{z},$$

where $\pi(\boldsymbol{z}) = \prod_{m=1}^M \prod_{d=1}^D \pi^m_d(z^m_d)$. Since the exact output cannot be computed, we introduce the MSCG and RB outputs defined as $s_h(\boldsymbol{z})$, $s_N(\boldsymbol{z})$ respectively. Moreover, we shall assume that $s_h(\boldsymbol{z})$ is indistinguishable from $s(\boldsymbol{z})$ for any $\boldsymbol{z} \in \Gamma$, and that $s_N(\boldsymbol{z})$ is computed by using a RB space of dimension $N$ in (18) for all subdomains. Since the RB approximation is constructed upon the MSCG approximation we expect a high statistical correlation between both outputs provided the basis is rich enough.

We now apply the above idea to compute an estimate of $E[s_h]$, where $s_h(\boldsymbol{z})$ is the stochastic output obtained by using the MSCG method to solve the underlying stochastic PDE. To achieve this goal, we introduce

$$s^*_h(\boldsymbol{z}) = s_h(\boldsymbol{z}) + (E[s_{N_1}] - s_{N_1}(\boldsymbol{z})),$$

where $s_{N_1}(\boldsymbol{z})$ is the RB output for some $N_1 \in [1, N_{\max}]$. Because $s_{N_1}(\boldsymbol{z})$ generally approximates $s_h(\boldsymbol{z})$ very well, the two outputs are highly correlated. The expectation may be recast as

$$E[s_h] = E[s^*_h] = E[s_h - s_N] + E[s_N]. \tag{19}$$

The underlying premise here is that the two expectation terms on the right hand side can be computed efficiently by MC simulations owing to variance reduction and model reduction: the first term requires a small number of samples because its variance is generally very small, while the second term is less expensive to evaluate because it involves the RB output. The numerical simulation of (19) is denoted as model and variance reduction (MVR) estimate of the expectation

$$E_{M_0,M_1}[s_h] = E_{M_0}[s_h - s_N] + E_{M_1}[s_N], \tag{20}$$

which is unbiased.

The application of the CLT enables us to derive *a posteriori* estimate for the error in the expectation, that is

$$\lim_{M_0\to\infty} \lim_{M_1\to\infty} \Pr\left(\left|E[s_h] - E_{M_0,M_1}[s_h]\right| \le \Delta^E_{M_0,M_1}\right) = \operatorname{erf}\left(\frac{a}{\sqrt{2}}\right), \tag{21}$$

$$\Delta^E_{M_0,M_1} = a\sqrt{\frac{V_{M_0}[s_h - s_{N_1}]}{M_0} + \frac{V_{M_1}[s_{N_1}]}{M_1}}, \tag{22}$$

where $a > 0$ is the confidence level. For instance, in order to guarantee that $\left|E[s_h] - E_{M_0,M_1}[s_h]\right|$ is bounded by a specified error tolerance $\epsilon_{\text{tol}}$ with a high probability (say, greater than 0.95), we need to take $a \ge 1.96$ according to the CLT. Similarly, the estimate of the variance is defined as

$$V_{M_0,M_1}[s_h] = E_{M_0}[\zeta_h - \zeta_{N_1}] + E_{M_1}[\zeta_{N_1}],$$

where the auxiliary variables are $\zeta_h := (s_h - E_{M_0,M_1}[s_h])^2$ and $\zeta_{N_1} := (s_{N_1} - E_{M_0,M_1}[s_h])^2$. The error bound for the variance is defined analogously. The above derivations, the extension to the multilevel context and the optimal choice of sample and RB sizes is thouroughly discussed and analyzed in [57].

### *3.4. Computation of gradients*

In the optimization context the usage of first order optimization algorithms usually leads to accelerated convergence to the optimum value, as it guarantees a more efficient exploration of the design space. We review now how to obtain the gradients for the MSCG method.

Following our assumptions, the vector of parameters $\boldsymbol{z}$ has at most dimension $MD$, since the defect subdomains do not require any parameter. We now derive an adjoint approach to compute gradients in the multiscale context. The solution to the MSCG problem in matrix form is $\mathbf{u} = \mathbf{U}_\varphi \boldsymbol{\Lambda} + \mathbf{U}_f$, where $\mathbf{U}_\varphi \in \mathbb{C}^{\mathcal{N}_\ell \times \mathcal{N}_g}$ is a matrix that contains the solutions to the Dirichlet subproblems and $\mathbf{U}_f$ is a vector of dimension $\mathcal{N}_\ell$ that contains the solution to the source problem.

If we are interested in a single output $s(\mathbf{u}, \boldsymbol{z})$, its derivatives can be computed as

$$\frac{ds}{d\boldsymbol{z}} = \frac{\partial s}{\partial \boldsymbol{z}} + \frac{\partial s}{\partial \mathbf{u}} \frac{\partial \mathbf{u}}{\partial \boldsymbol{z}} = \frac{\partial s}{\partial \boldsymbol{z}} + \frac{\partial s}{\partial \mathbf{u}} \left( \frac{\partial \mathbf{U}_f}{\partial \boldsymbol{z}} + \frac{\partial \mathbf{U}_\varphi}{\partial \boldsymbol{z}} \boldsymbol{\Lambda} + \mathbf{U}_\varphi \frac{\partial \boldsymbol{\Lambda}}{\partial \boldsymbol{z}} \right).$$

We invoke the adjoint technique to solve the last part, namely

$$\frac{\partial s}{\partial \mathbf{u}} \mathbf{U}_\varphi \frac{\partial \boldsymbol{\Lambda}}{\partial \boldsymbol{z}} = \frac{\partial s}{\partial \mathbf{u}} \mathbf{U}_\varphi \mathbb{K}^{-1} \left( \frac{\partial \mathbb{F}}{\partial \boldsymbol{z}} - \frac{\partial \mathbb{K}}{\partial \boldsymbol{z}} \boldsymbol{\Lambda} \right) = \psi^\dagger \left( \frac{\partial \mathbb{F}}{\partial \boldsymbol{z}} - \frac{\partial \mathbb{K}}{\partial \boldsymbol{z}} \boldsymbol{\Lambda} \right),$$

where the adjoint variable is the solution of

$$\mathbb{K}^\dagger \psi = \left( \frac{\partial s}{\partial \mathbf{u}} \mathbf{U}_\varphi \right)^\dagger,$$

thus allowing us to compute the (at most) $MD$ derivatives with only an extra adjoint solution.

The derivatives of $\mathbf{U}_\varphi$, $\mathbf{U}_\mathbf{f}$, $\mathbb{K}$, $\mathbb{F}$ with respect to $\boldsymbol{z}$ are sparse since the parameters only have local influence, and can be evaluated with (12),(7b) and (11) for the MSCG case and with (17) and (18) for the RB case. An additional advantage of RB is the computation of these derivatives, since the affine dependence on the parameters that arises from the DEIM greatly simplifies the computation.

## 4. Numerical results

### *4.1. Convergence test and cost analysis*

Firstly, we study the convergence of the MSCG and compare it to that of the standard CG for a simple problem. The problem is to solve (1) in a unit square $\Omega = (0,1)^2$ for $\rho = \kappa^2 = 1$, where the Dirichlet condition and source term are chosen such that the exact solution is

$$u(\mathbf{x}) = x^2 + y^2 + \sin(k(x\cos\theta + y\sin\theta)).$$

The exact solution is a planewave of wavenumber $k$ propagating in the $\theta$ direction. The results reported here correspond to $\theta = \pi/4$ and $k = 6$.

For the CG discretization, we consider a homogeneous triangulation of $2n^2$ elements with uniform element size of $h = 1/n$. For the MSCG, we subdivide the domain into $q^2$ uniform squares, each of them with $2n^2/q^2$ triangles of uniform element size of $h = q/n$. To represent the solution we consider both polynomial order $p = 1, 2$ for all subdomains; for the interfaces, besides considering a polynomial order sufficient to capture the frequency of the problem, for instance 10, we also require for any boundary face that the local discretization is finer than the global discretization in order to capture the boundary conditions prescribed by the Lagrange polynomial. Hence we take $p^\mathsf{f} = \min\{10, np/q\}$, and discretize each global face with a single high-order element.

We compute the $L^2(\Omega)$ errors for both methods for $n = 8, 16, 32, 64, 128$ and $q = 1, 2, 4, 8$ for the subdivisions, and the results are collected in Table 1 for $p = 1$ and Table 2 for $p = 2$. The errors for both methods coincide, and yield the expected convergence rate of $\mathcal{O}(h^{p+1})$ for smooth solutions. Indeed, as long as the global polynomial order suffices for the frequency of interest, the error will be dominated by the subproblems, where both methods have the same discretization.

| **Mesh** | **MSCG error** | | | | **CG error** | **Order** |
|---|---|---|---|---|---|---|
| $n$ | $q = 1$ | $q = 2$ | $q = 4$ | $q = 8$ | | |
| 8 | 2.80e-2 | 2.80e-2 | 2.80e-2 | 2.80e-2 | 2.80e-2 | – |
| 16 | 7.63e-3 | 7.63e-3 | 7.63e-3 | 7.63e-3 | 7.63e-3 | 1.86 |
| 32 | 1.96e-3 | 1.96e-3 | 1.96e-3 | 1.96e-3 | 1.96e-3 | 1.97 |
| 64 | 4.92e-4 | 4.92e-4 | 4.92e-4 | 4.92e-4 | 4.92e-4 | 1.99 |
| 128 | 1.23e-4 | 1.23e-4 | 1.23e-4 | 1.23e-4 | 1.23e-4 | 2.00 |

Table 1: $L^2(\Omega)$ error and convergence rate for MSCG and CG for $p = 1$ as a function of $n$.

| **Mesh** | **MSCG error** | | | | **CG error** | **Order** |
|---|---|---|---|---|---|---|
| $n$ | $q = 1$ | $q = 2$ | $q = 4$ | $q = 8$ | | |
| 8 | 6.23e-4 | 6.23e-4 | 6.23e-4 | 6.23e-4 | 6.23e-4 | – |
| 16 | 7.55e-5 | 7.55e-5 | 7.55e-5 | 7.55e-5 | 7.55e-5 | 3.04 |
| 32 | 9.38e-6 | 9.38e-6 | 9.38e-6 | 9.38e-6 | 9.38e-6 | 3.01 |
| 64 | 1.17e-6 | 1.17e-6 | 1.17e-6 | 1.17e-6 | 1.17e-6 | 3.00 |
| 128 | 1.46e-7 | 1.46e-7 | 1.46e-7 | 1.46e-7 | 1.46e-7 | 3.00 |

Table 2: $L^2(\Omega)$ error and convergence rate for MSCG and CG for $p = 2$ as a function of $n$.

Another relevant study is the comparison of degrees of freedom for both methods. A uniform triangular mesh of $2n^2$ elements of order $p$ renders $\mathcal{N}_{CG} = (np + 1)^2$ high-order nodes. Conversely, for each of the $q^2$ subdomains of the MSCG we have $2(n/q)^2$ elements and $\mathcal{N}_\ell = (np/q+1)^2$ degrees of freedom. Furthermore, if we assume a homogeneous polynomial order $p^{\mathsf{f}}$ for the Lagrange polynomial at the interfaces, it can be shown that $\mathcal{N}_g = (q + 1)(2qp^{\mathsf{f}} - q + 1)$. If we adopt $p^{\mathsf{f}} = \min\{10, np/q\}$, which suffices to represent the solution accurately for this case, we obtain the degrees of freedom presented in Table 3 for $p = 2$.

| **Mesh** | **MSCG** | | | | | | **CG** |
|---|---|---|---|---|---|---|---|
| $n$ | $q = 2$ | | $q = 4$ | | $q = 8$ | | |
| | $\mathcal{N}_\ell$ | $\mathcal{N}_g$ | $\mathcal{N}_\ell$ | $\mathcal{N}_g$ | $\mathcal{N}_\ell$ | $\mathcal{N}_g$ | $\mathcal{N}_{CG}$ |
| 8 | 81 | 93 | 25 | 145 | 9 | 225 | 289 |
| 16 | 289 | 117 | 81 | 305 | 25 | 513 | 1089 |
| 32 | 1089 | 117 | 289 | 385 | 81 | 1089 | 4225 |
| 64 | 4225 | 117 | 1089 | 385 | 289 | 1377 | 16641 |
| 128 | 16641 | 117 | 4225 | 385 | 1089 | 1377 | 66049 |

Table 3: Degrees of freedom for MSCG and CG for $p = 2$ as a function of $n$.

This analysis shows that, for this problem where there is only one subdomain type, the best strategy is to use more subdivisions per direction as we reduce the mesh size. Indeed, a multiscale configuration is deemed optimal whenever the degrees of freedom for both the local and global problem are in the same order of magnitude, thus the computational burden is divided evenly. Furthermore, notice that the benefit of the MSCG as opposed to regular CG becomes apparent as more elements are used in the discretization. The results presented here correspond to the very simple case where only one local computation needs to be performed, therefore if there is more than one subdomain type one needs to account for the multiple unique local subproblems. However, if the several subdomain types are then solved in parallel the cost can be assumed proportional to a single local solve, which greatly benefits the efficiency of the MSCG method.

| type | # elements | order | $\mathcal{N}_\ell$ | # subdomains | # dof |
|---|---|---|---|---|---|
| 1 | 9460 | 2 | 19K | 613 | 12M |
| 2 | 4050 | 2 | 8K | 50 | 0.4M |
| 3 | 4050 | 2 | 8K | 663 | 5.5M |
| Global | 2729 | 10 | 11 | 1326 | 26K |

Table 4: Degrees of freedom for MSCG for the waveguide splitter separated by subdomain types.

### *4.2. Deterministic waveguide simulation*

We now focus on the simulation of waveguiding through photonic crystals, a feature widely used in telecommunications and optical wave control. Photonic crystals are structured materials that are assembled by combining different materials respecting the symmetries of the square or the hexagon, giving rise to a periodic nanostructure that exhibits the bandgap phenomenon. That is, there exists broad bands of frequencies for which wave propagation through the crystal is exponentially decaying. Common examples of such structures are dielectric rods in air or holes drilled in a dielectric slab, and its bandgaps have been extensively studied [28]. Waveguiding arises as an application of photonic crystals whenever symmetry of the lattice is broken, for instance when a line of rods is removed from the crystal. In this scenario, if the crystal is illuminated with a wave whose frequency is in the gap, the wave will only be allowed to travel along the defect, as it will be evanescent away from the defect due to the exponential decay. The MSCG presented in this paper is therefore an attractive candidate to simulate photonic crystal applications, since they rely on the repetition of patterns on a lattice structure. Thus, the nature of the MSCG method will enable us to simulate large photonic crystal structures by computing only a handful of different subproblems.

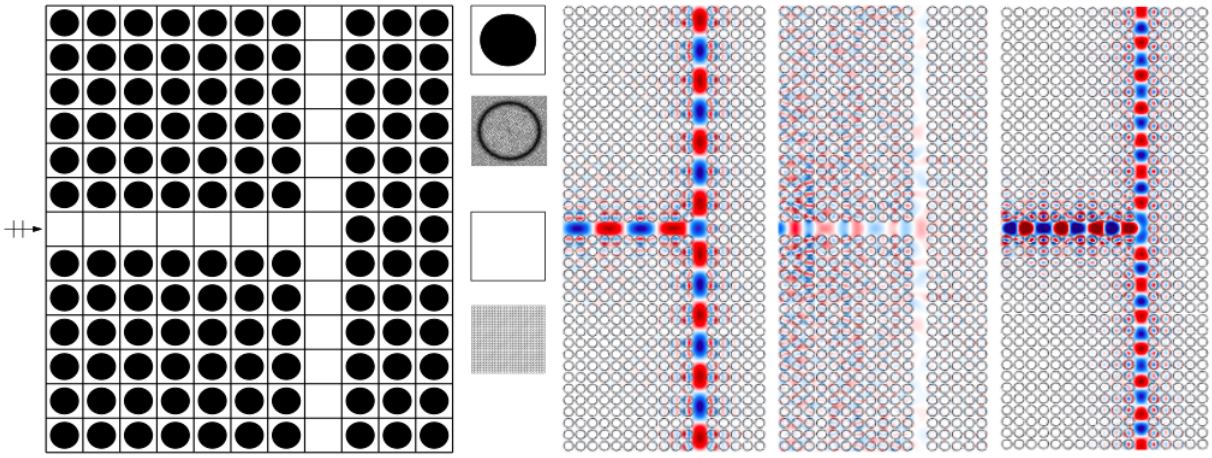

Figure 4: MSCG simulation of a TM waveguide splitter of GaAs rods ($\varepsilon = 11.4$) in air. Computational domain with subdomain decomposition (excluding PMLs) and meshes (left). Numerical simulation at frequencies $\omega a/2\pi c = 0.39$, $\omega a/2\pi c = 0.46$ and $\omega a/2\pi c = 0.53$ (left to right).

The first example is a waveguide splitter consisting of Gallenium Arsenide rods ($\varepsilon = 11.4$) in air of radius $R_0 = 0.4a$, where $a$ is the periodicity of the crystal. For the TM polarization, this structure presents a first bandgap for $\omega a/2\pi c \in (0.36, 0.40)$ and a second bandgap for $\omega a/2\pi c \in (0.52, 0.55)$. In order to numerically simulate the splitter with the MSCG, we first have to identify the subdomains in which to split the computational domain. The subdomains should be invariant to rotation and translation to ensure a small number of subproblems are solved. The size of the subdomain along with the frequencies of interest determine the polynomial order chosen to approximate the solution at the global interfaces. Conversely, the discretization needed at the subdomain level is governed by the details of the geometry together with the

frequency of the propagating wave. Furthermore, the MSCG gives rise to the possibility of using different polynomial approximation order for different subdomains, which can greatly impact its efficiency.

For the waveguide splitter shown in Figure 4 (left), we choose three different types of subdomains: (1) the rod subdomain, where we use $p = 2$, curved elements and adaptive mesh size to approximate the fine detail of the rod curvature; (2) the defect subdomain, where we use an homogeneous mesh of straight-sided elements of order $p = 2$; and (3) the PML subdomain, with the same discrtization as type 2 but where we solved the modified Helmholtz equation given by (2). For each global interface we choose a single element of polynomial order $p^{\mathsf{f}} = 10$, which gives sufficient resolution of more than 20 points per wavelength. The degree of freedom count is reported in Table 4. Note that solving the exact same problem with regular CG would suppose solving a linear system of more than 18M dof as oposed to a system of 26K dof, thus the competitive advantage of MSCG is clear for problems presenting such a repetitive structure.

In Figure 4 (right) we show the amplitude field for a frequency in the first bandgap, a frequency between the two bandgaps and a frequency in the second bandgap. An attractive feature of waveguiding with photonic crystals are the low losses that occur even for sharp bends, thus enabling the efficient guiding or splitting of electromagnetic waves, as it can be observed for frequencies in the bandgap.

### *4.3. Deterministic waveguide optimization*

Let us consider the simulation and design of a photonic crystal consisting of a silicon ($\varepsilon = 12.1$) slab assembled in a triangular lattice with drilled air holes of radius $R_0 = 275a/800$, which presents a broad bandgap for $\omega a/2\pi c \in (0.26, 0.34)$ for TE waves, see [18]. A waveguide is generated by opening a defect with two 60° bends according to the symmetry of the lattice and illuminating the crystal with a wave impinging at the input port. The quantity of interest is the intensity of the optical power at the output port in the $x$-direction, namely

$$s_h = \frac{1}{2\omega} \sum_{i=1}^{I} \Big| \int_{\Omega^i_{out}} \rho \mathbf{e}_x \cdot \Re \left[ iu \nabla u^\dagger \right] \Big|,$$

where the subdomains at the output port comprise the line defect and one rod subdomain above and below according to the symmetry of the lattice. The schematics of the slab are shown in Figure 5a (left), where we have ensured that the bends are sufficiently separated such that they do not interact. The objective here is to apply the methdology above to find a design for the bending region such that guarantees transmission for certain frequencies of interest, since the waveguide only transmits very narrow bands of frequencies within the bandgap [18], see Figure 5b.

Firstly, we describe the different subdomains that can be identified, see Figure 5a (right). The subdomain types 1 and 2 correspond both the the subdomain with a rod and triangular symmetry, but are treated independently since the subdomains pertaining to type 1 will be subject to shape optimization, whereas the subdomains from type 2 remain undeformed. The other two subdomain types correspond to the line defect and the PML respectively. The dof count for the different types and the global problem is collected in Table 5.

| **type** | **# elements** | **order** | $\mathcal{N}_\ell$ | **# subdomains** | **# dof** |
|---|---|---|---|---|---|
| 1 | 9196 | 2 | 19K | 58 | 1M |
| 2 | 9196 | 2 | 19K | 607 | 11M |
| 3 | 4050 | 2 | 8K | 37 | 0.3M |
| 4 | 4050 | 2 | 8K | 482 | 4M |
| Global | 2437 | 10 | 11 | 1184 | 23K |

Table 5: Degrees of freedom for MSCG for the 60° double waveguide bend separated by subdomain types.

In this paper we only consider shape optimization, as opposed topology optimization described in [4]. The optimization variables are the radii of the rods in type 1. Hence, we have $M_1 = 58$ design parameters $\theta^m$

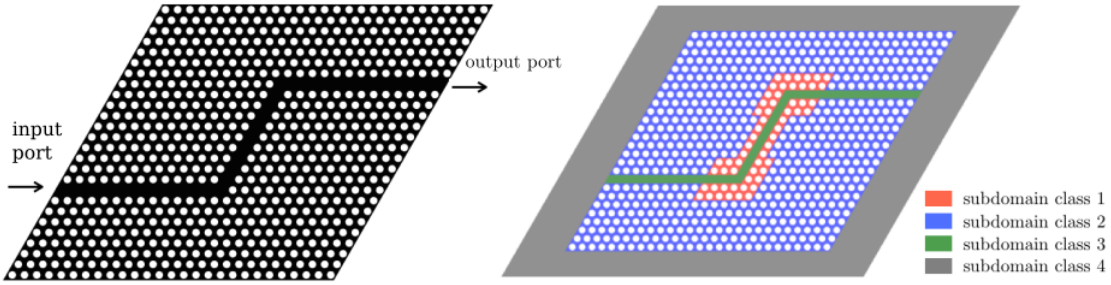


(a) Left: Silicon slab with two consecutive 60° bends on a triangular lattice. Right: Computational domain with different subdomains highlighted. The red subdomains correspond to rods in the optimization area.

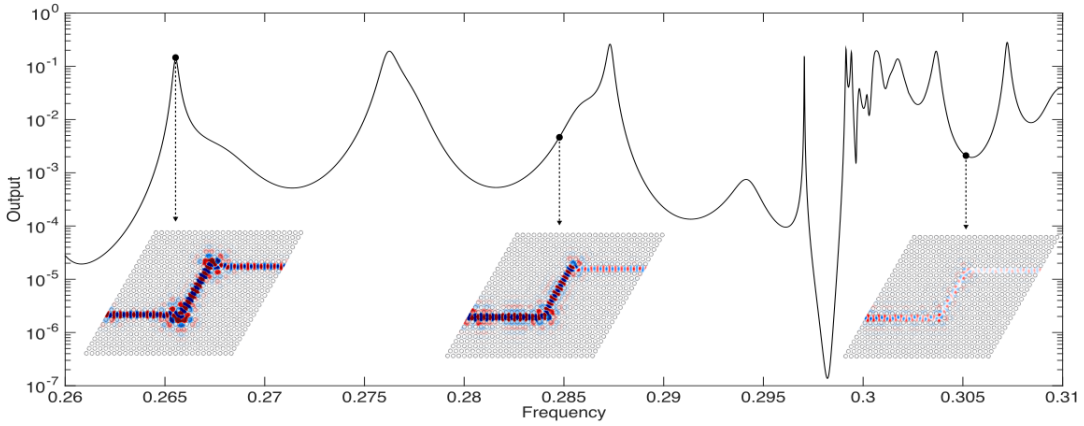


(b) Quantity of interest vs frequency, with amplitude field shown for $\omega a/2\pi c = \{0.2655, 0.285, 0.305\}$.

Figure 5: Schematics, computational domain and solutions for the silicon slab wave propagation problem.

defined as $r_0^m = R_0(1+\theta^m)$, $1 \leq m \leq M_1$. Box constraints are prescribed for all design parameters with limits $\theta^m \in [-0.127, 0.047]a$ such that $r^m \in [0.3, 0.36]a$. Thus, the required mapping $\mathfrak{G}^1$ deforms the circular surface of the hole continuously by leaving the boundaries of the subdomain and a small region around the center (to avoid the singularity) fixed, such that the deformed surface of the hole achieves the desired radius value. The mapping for the other subdomain types is the identity.

The first step towards efficient optimization is to develop a RB for the subdomains of type 1, which reduces to finding a RB for the Dirichlet subproblem (12) as we have no source. The application of the DEIM on the three components of $\boldsymbol{G}$ (represents a second-order symmetric tensor) and the jacobian $g$ enables the affine parametrization of the mapping, for a total of $Q = 6$ and $K = 4$ interpolation elements, guaranteeing the error in the RB is not dominated by the empirical interpolation. We then compute snapshots to (12) for the multiple Dirichlet conditions, where the parameters are $\theta$ and the frequency $\omega$ –thus the RB can be reused at multiple frequencies. Finally, the RB is constructed by compressing the snapshots for all the boundary conditions on a single POD basis, weighted by the energy norm of the problem.

We now proceed to optimizing the radii of the rods. The deterministic optimization problem reads

$$s_h^*(\boldsymbol{\theta}^*) = \max_{\boldsymbol{\theta} \in \boldsymbol{\Theta}} s_h, \tag{23}$$

where $\boldsymbol{\Theta}$ is the design region. The optimization algorithm used is multi-level single linkage [32, 33] for global optimization combined with preconditioned truncated Newton [16] for local optimization, both implemented in the `nlopt` [30] optimization package. The first results correspond to a single frequency optimization, in this case $\omega a/2\pi c = 0.305$, for which transmission is poor. Since the frequency is constant, we precompute

(11) and (12) for types 2, 3 and 4, thus for each new $\boldsymbol{\theta}$ we only need to solve for the 58 subdomains from type 1. Moreover, we shall substitute the expensive CG local solution (11)-(12) for the inexpensive RB counterpart (17)-(18) to greatly accelerate the computations, which corresponds to solving (23) replacing $s_h$ by $s_N$. In the present case we use a reduced basis of size $N = 100$ that produces the solution to the local problem 150 faster than standard CG. The relative error of $s_N(\boldsymbol{\theta}^*)$ with respect to $s_h(\boldsymbol{\theta}^*)$ is $2.3e-5$, hence certifying the accuracy of the RB and validating the approach. The quantity of interest for the optimal radius variation $\boldsymbol{\theta}^*$ is shown in Figure 6a (dashed red) for several frequencies, showing a much higher transmission than the un-optimized version, see Figure 5b.

### *4.4. Robust waveguide optimization*

The next step is to seek a design that is robust with respect to a range of frequencies, which is desirable when the optimum presents a sharp peak with a rapid decay for small variations. This optimization problem can be recast in a stochastic optimization framework as

$$\widehat{s}_h(\widehat{\boldsymbol{\theta}}) = \max_{\boldsymbol{\theta}\in\boldsymbol{\Theta}} E_\omega[s_h] - \gamma\sqrt{V_\omega[s_h]} \tag{24}$$

where $\gamma$ controls the weight assigned to the variance minimization. Since the stochastic space is unidimensional, the output statistics can be computed with simple Gauss-Legendre quadrature, reducing (24) to the weighted evaluation of the output at the frequencies given by Legendre points. Thus, we can again precompute (11)-(12) for types 2, 3 and 4 at the required frequencies in the range $\omega a/2\pi c = [0.3045, 0.3055]$. The value of the output for the minimizer $\widehat{\boldsymbol{\theta}}$ (dashed green) for $\gamma = 1$ is shown in Figure 6a for several discrete frequencies. Robustness with respect to frequency variations is achieved for design $\widehat{\boldsymbol{\theta}}$ in comparison to the deterministic optimum $\boldsymbol{\theta}^*$ (dashed red).

Finally, we analyze the robustness of the solutions with respect to geometry errors for a range of frequencies. The geometry errors, which will be considered for subdomains in types 1 and 2, are given by (13), where we append the constant deformation $\theta^m$ for the optimization, namely $r_0^m \to R_0^m\,[1+\theta^m]+\delta R_0^m$. For the results below, we select $D = 11$, $\sigma = 0.02$, $L_c = 1/16$ and $\boldsymbol{z}^m \in [-\sqrt{3},\sqrt{3}]^D$, for which the 95% confidence interval gives $\left|\delta R_0^m\right|/R_0^m < 3\%$ if $\theta = 0$. Note we encapsulate both the optimization and the stochastic parameters in the same expression, and thus use the same RB for both types of subdomains by simply setting $\theta^m = 0$ for the subdomains in type 2.

In order to achieve robust designs accounting for variation in both the frequency and the geometry parameters, we formulate the following stochastic optimization problem

$$\widetilde{s}_h(\widetilde{\boldsymbol{\theta}}) = \max_{\boldsymbol{\theta}\in\boldsymbol{\Theta}} E_{\omega,\mathcal{G}}[s_h] - \gamma\sqrt{V_{\omega,\mathcal{G}}[s_h]}. \tag{25}$$

The stochastic dimension of the problem under consideration is enormous, since we have 11 geometry parameters per subdomain plus the frequency, and there are 665 subdomains of types 1 and 2 combined. Hence, we shall resort to the MVR method described in Section 3.3 to compute the statistics of the quantity of interest. We develop a RB using the DEIM combined with POD for the non-homogeneous radius variation. We set $\theta^m \in [-0.127, 0.047]a$ as before for the optimization, which in this case leads to $Q = 61$ and $K = 23$ elements in the interpolation basis. We again use $N = 100$ for the RB model, which leads to a reduction in variance of more than two orders of magnitude when evaluated on a random set of realizations of $\boldsymbol{z}$ for the design $\widehat{\boldsymbol{\theta}}$. This RB is less accurate than the one developed for $\boldsymbol{\theta}$ only, since have considered 11 additional parameters to represent the geometry and we use the same RB size. The main difference here is that we employ the RB as a surrogate that correlates with the high-fidelity model, not as a substitute, thus a coarser basis still casts excellent results.

In Figure 6a we show in dashed line, for a set of discrete frequencies in the interval $\omega a/2\pi c = [0.3045, 0.3055]$, the transmission $s_h$ for the several configurations considered: single frequency optimization $\boldsymbol{\theta}^*$, range of frequencies $\widehat{\boldsymbol{\theta}}$ and robust design $\widetilde{\boldsymbol{\theta}}$. We compare the results with $E_{\mathcal{G}}[s_h(\boldsymbol{\theta})]\pm\Delta^E$, computed with (20)-(21), for

several frequencies within the interval. The single frequency optimum $\boldsymbol{\theta}^*$ produces the highest transmission for $\omega a/2\pi c = 0.305$, but it degrades significantly in the presence of geometric errors. Conversely, the other optima, albeit attaining lower peak transmission values, maintain a satisfactory performance for all the frequencies in the range. Moreover, the robust optimum outperforms the range of frequencies optimum both in expected value and in variance, see Figure 6b. These results show the importance of accounting for the geometry variations in the objective function if robust designs are sought. Finally, in Figure 6c we depict the several optima $\boldsymbol{\theta}$, expressed as a variation on the nominal radius, for the three different scenarios considered.

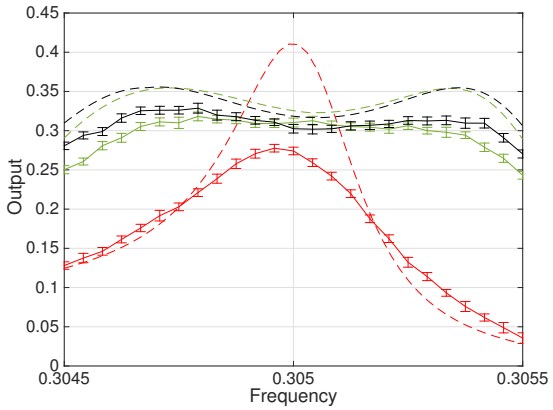


(a) Output for no geometric errors (dashed) and expected value of output with respect to geometry with 95% confidence interval (solid) for the three optimized designs at single frequencies.

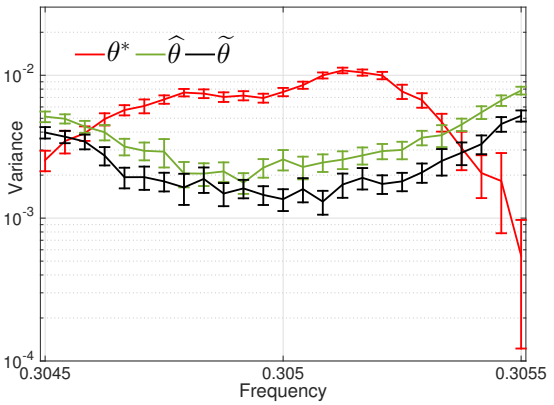


(b) Variance of output with respect to geometry with 95% confidence interval for the three optimized designs at single frequencies.

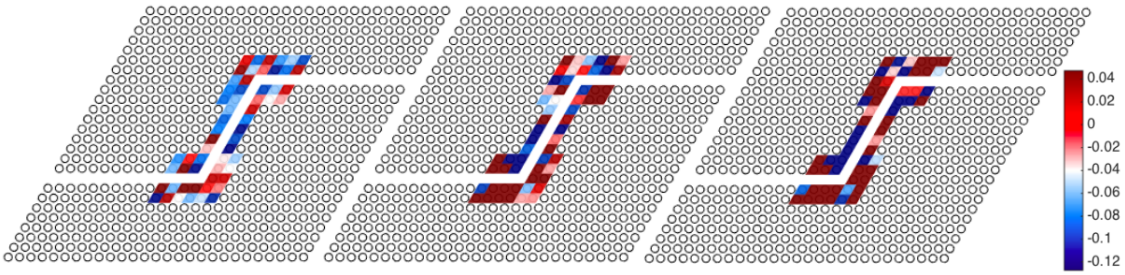


(c) Single frequency $\boldsymbol{\theta}^*$ (left), range of frequencies $\widehat{\boldsymbol{\theta}}$ (middle) and robust design $\widetilde{\boldsymbol{\theta}}$ (right) optima.

Figure 6: Results for the robust optimization problem.

## 5. Conclusions

We have presented a multiscale continuous Galerkin method for computing wave propagation phenomena through heterogeneous materials. The method relies on partitioning the computational domain into subdomains, and computing the local solution at the subdomain as a function of the Lagrange multipliers at the interfaces. Thus, we statically condensate the local problem to the global degrees of freedom and solve a linear system for the Lagrange multipliers only. We then recover the solution in the interior of the subdomain by linearity and superposition. Furthermore, the MSCG is especially advantageous for problems that exhibit repeated patterns, since the local subproblems may be reused for similar subdomains. This methodology is implemented together with a reference domain formulation that allows us to consistently model geometric deformations at the subdomain level. In addition, we propose the construction of a reduced order model

for the local subproblems to speed up the MSCG method. We then use the model and variance reduction method to compute statistical outputs of stochastic wave propagation problems. Finally, we presented a convergence test to verify the convergence rate of MSCG, a deterministic simulation of a waveguide splitter to illustrate the advantages of MSCG in photonic crystal, and a robust optimization of a photonic slab to demonstrate the performance of MSCG for robust designs.

We conclude the paper by pointing out several possible extensions for further research. Firstly, it would be interesting to address model reduction at the global level [17]. In the two dimensional examples introduced here the computational burden is usually concentrated at the subdomain level, but for three dimensional cases it is imperative to minimize not only the size of the global problem, but also the amount of Dirichlet problems that need to be solved at each subdomain. Furthermore, we would like to extend this approach for the time-harmonic Maxwell's equations in three dimensions. The challenges are threefold: (1) the development of a consistent reference domain formulation is not as straightforward as for the Helmholtz equation; (2) the vector nature of Maxwell's equation increases the computational cost as it requires solving for multiple components of the solution field; and (3) as mentioned earlier, the interfaces are approximated by two-dimensional Lagrange polynomials, thus squaring the amount of Dirichlet subproblems required for the subdomain types. Nonetheless, the ultimate goal is to develop the methodology just described to tackle plasmonic problems [13, 26, 44], which involve not only full 3d simulations but also tremendous mismatchs in length scales.

## Acknowledgements

We would like to thank Dr. Xevi Roca and Professor Anthony Patera for useful conversations, suggestions and comments.

## References

[1] Aarnes, J., Heimsund, B.-O., 2005. Multiscale discontinuous Galerkin methods for elliptic problems with multiple scales. In: Multiscale methods in science and engineering. Springer, pp. 1–20.

[2] Ainsworth, M., Coyle, J., 2003. Hierarchic finite element bases on unstructured tetrahedral meshes. International Journal for Numerical Methods in Engineering 58 (14), 2103–2130.

[3] Barrault, M., Maday, Y., Nguyen, N.-C., Patera, A. T., 2004. An 'empirical interpolation' method: application to efficient reduced-basis discretization of partial differential equations. Comptes Rendus Mathematique 339 (9), 667–672.

[4] Bendsoe, M. P., Sigmund, O., 2013. Topology optimization: theory, methods, and applications. Springer Science & Business Media.

[5] Bensoussan, A., Lions, J.-L., Papanicolaou, G., 2011. Asymptotic analysis for periodic structures. Vol. 374. American Mathematical Soc.

[6] Berenger, J.-P., 1994. A perfectly matched layer for the absorption of electromagnetic waves. Journal of computational physics 114 (2), 185–200.

[7] Berkooz, G., Holmes, P., Lumley, J. L., 1993. The proper orthogonal decomposition in the analysis of turbulent flows. Annual review of fluid mechanics 25 (1), 539–575.

[8] Bernardi, C., 1994. A new nonconforming approach to domain decomposition: the mortar element method. Nonliner Partial Differential Equations and Their Applications.

[9] Bernardi, C., Maday, Y., Patera, A. T., 1993. Domain decomposition by the mortar element method. In: Asymptotic and numerical methods for partial differential equations with critical parameters. Springer, pp. 269–286.

[10] Casadei, F., Rimoli, J., Ruzzene, M., 2013. A geometric multiscale finite element method for the dynamic analysis of heterogeneous solids. Computer Methods in Applied Mechanics and Engineering 263, 56–70.

[11] Chaturantabut, S., Sorensen, D. C., 2010. Nonlinear model reduction via discrete empirical interpolation. SIAM Journal on Scientific Computing 32 (5), 2737–2764.

[12] Chen, P., Quarteroni, A., Rozza, G., 2014. Comparison between reduced basis and stochastic collocation methods for elliptic problems. Journal of Scientific Computing 59 (1), 187–216.

[13] Chen, X., Park, H.-R., Pelton, M., Piao, X., Lindquist, N. C., Im, H., Kim, Y. J., Ahn, J. S., Ahn, K. J., Park, N., et al., 2013. Atomic layer lithography of wafer-scale nanogap arrays for extreme confinement of electromagnetic waves. Nature communications 4.

[14] Chen, Z., Hou, T., 2003. A mixed multiscale finite element method for elliptic problems with oscillating coefficients. Mathematics of Computation 72 (242), 541–576.

[15] Cockburn, B., Gopalakrishnan, J., Wang, H., 2007. Locally conservative fluxes for the continuous Galerkin method. SIAM Journal on Numerical Analysis 45 (4), 1742–1776.
[16] Dembo, R. S., Steihaug, T., 1983. Truncated-Newton algorithms for large-scale unconstrained optimization. Mathematical Programming 26 (2), 190–212.
[17] Eftang, J. L., Patera, A. T., 2013. Port reduction in parametrized component static condensation: approximation and a posteriori error estimation. International Journal for Numerical Methods in Engineering 96 (5), 269–302.
[18] Frandsen, L. H., Harpøth, A., Borel, P. I., Kristensen, M., Jensen, J. S., Sigmund, O., 2004. Broadband photonic crystal waveguide 60 bend obtained utilizing topology optimization. Optics Express 12 (24), 5916–5921.
[19] Frei, W., Johnson, H., 2004. Finite-element analysis of disorder effects in photonic crystals. Physical Review B 70 (16), 165116.
[20] Giles, M. B., 2008. Multilevel Monte Carlo path simulation. Operations Research 56 (3), 607–617.
[21] Graglia, R. D., Wilton, D. R., Peterson, A. F., 1997. Higher order interpolatory vector bases for computational electromagnetics. IEEE Transactions on Antennas and Propagation 45 (3), 329–342.
[22] Hou, T., Wu, X.-H., Cai, Z., 1999. Convergence of a multiscale finite element method for elliptic problems with rapidly oscillating coefficients. Mathematics of Computation of the American Mathematical Society 68 (227), 913–943.
[23] Hou, T. Y., Wu, X.-H., 1997. A multiscale finite element method for elliptic problems in composite materials and porous media. Journal of computational physics 134 (1), 169–189.
[24] Huynh, D., Knezevic, D. J., Patera, A. T., 2013. A static condensation reduced basis element method: approximation and a posteriori error estimation. ESAIM: Mathematical Modelling and Numerical Analysis 47 (01), 213–251.
[25] Huynh, D., Knezevic, D. J., Patera, A. T., 2013. A static condensation reduced basis element method: Complex problems. Computer Methods in Applied Mechanics and Engineering 259, 197–216.
[26] Im, H., Lindquist, N. C., Lesuffleur, A., Oh, S.-H., 2010. Atomic layer deposition of dielectric overlayers for enhancing the optical properties and chemical stability of plasmonic nanoholes. Acs Nano 4 (2), 947–954.
[27] Jin, J.-M., 2014. The finite element method in electromagnetics. John Wiley & Sons.
[28] Joannopoulos, J. D., Johnson, S. G., Winn, J. N., Meade, R. D., 2011. Photonic crystals: molding the flow of light. Princeton university press.
[29] Johnson, S. G., 2008. Notes on perfectly matched layers (PMLs). Lecture notes, Massachusetts Institute of Technology, Massachusetts 5 (5.3), 2.
[30] Johnson, S. G., http://ab-initio.mit.edu/nlopt. The NLopt nonlinear-optimization package.
[31] Johnson, S. G., Fan, S., Villeneuve, P. R., Joannopoulos, J., Kolodziejski, L., 1999. Guided modes in photonic crystal slabs. Physical Review B 60 (8), 5751.
[32] Kan, A. R., Timmer, G. T., 1987. Stochastic global optimization methods part i: Clustering methods. Mathematical programming 39 (1), 27–56.
[33] Kan, A. R., Timmer, G. T., 1987. Stochastic global optimization methods part ii: Multi level methods. Mathematical Programming 39 (1), 57–78.
[34] Kanouté, P., Boso, D., Chaboche, J., Schrefler, B., 2009. Multiscale methods for composites: a review. Archives of Computational Methods in Engineering 16 (1), 31–75.
[35] Knight, J., Birks, T., Russell, P. S. J., Atkin, D., 1996. All-silica single-mode optical fiber with photonic crystal cladding. Optics letters 21 (19), 1547–1549.
[36] Kunz, K. S., Luebbers, R. J., 1993. The finite difference time domain method for electromagnetics. CRC press.
[37] Lidorikis, E., Sigalas, M., Economou, E. N., Soukoulis, C., 2000. Gap deformation and classical wave localization in disordered two-dimensional photonic-band-gap materials. Physical Review B 61 (20), 13458.
[38] Luo, C., Johnson, S. G., Joannopoulos, J., Pendry, J., 2002. All-angle negative refraction without negative effective index. Physical Review B 65 (20), 201104.
[39] Ng, L. W., Huynh, D. B., Willcox, K., 2012. Multifidelity Uncertainty Propagation for Optimization Under Uncertainty. In: 12th AIAA Aviation Technology, Integration, and Operations (ATIO) Conference and 14th AIAA/ISSMO Multidisciplinary Analysis and Optimization Conference.
[40] Nguyen, C., Roca, X., Moro, D., Peraire, J., 2013. A hybridized multiscale discontinuous Galerkin method for compressible flows. In: 51st AIAA Aerospace Sciences Meeting including the New Horizons Forum and Aerospace Exposition. p. 689.
[41] Nguyen, N. C., 2008. A multiscale reduced-basis method for parametrized elliptic partial differential equations with multiple scales. Journal of Computational Physics 227 (23), 9807–9822.
[42] Noor, A. K., Peters, J. M., 1980. Reduced basis technique for nonlinear analysis of structures. AIAA Journal 18 (4), 455–462.
[43] Oskooi, A. F., Roundy, D., Ibanescu, M., Bermel, P., Joannopoulos, J., Johnson, S. G., 2010. MEEP: A flexible free-software package for electromagnetic simulations by the FDTD method. Computer Physics Communications 181 (3), 687–702.
[44] Park, H.-R., Chen, X., Nguyen, N.-C., Peraire, J., Oh, S.-H., 2015. Nanogap-enhanced terahertz sensing of 1 nm thick ($\lambda/106$) dielectric films. ACS Photonics 2 (3), 417–424.
[45] Pendry, J. B., 2000. Negative refraction makes a perfect lens. Physical review letters 85 (18), 3966.
[46] Persson, P.-O., Bonet, J., Peraire, J., 2009. Discontinuous Galerkin solution of the Navier–Stokes equations on deformable domains. Computer Methods in Applied Mechanics and Engineering 198 (17), 1585–1595.
[47] Prudhomme, C., Rovas, D. V., Veroy, K., Machiels, L., Maday, Y., Patera, A. T., Turinici, G., 2002. Reliable real-time solution of parametrized partial differential equations: Reduced-basis output bound methods. Journal of Fluids Engineering 124 (1), 70–80.
[48] Rodriguez, A., Ibanescu, M., Joannopoulos, J. D., Johnson, S. G., 2005. Disorder-immune confinement of light in photonic-

crystal cavities. Optics letters 30 (23), 3192–3194.
[49] Rozza, G., Huynh, D., Patera, A. T., 2008. Reduced basis approximation and a posteriori error estimation for affinely parametrized elliptic coercive partial differential equations. Archives of Computational Methods in Engineering 15 (3), 229–275.
[50] Russell, P., 2003. Photonic crystal fibers. science 299 (5605), 358–362.
[51] Sadiku, M. N., 2000. Numerical techniques in electromagnetics. CRC press.
[52] Saleh, B. E., Teich, M. C., Saleh, B. E., 1991. Fundamentals of photonics. Vol. 22. Wiley New York.
[53] Sigalas, M., Soukoulis, C., Economou, E., Chan, C. T., Ho, K., 1993. Photonic band gaps and defects in two dimensions: Studies of the transmission coefficient. Physical Review B 48 (19), 14121.
[54] Sullivan, D. M., 2013. Electromagnetic simulation using the FDTD method. John Wiley & Sons.
[55] Taflove, A., Hagness, S. C., 2005. Computational electrodynamics. Artech house.
[56] Vidal-Codina, F., Nguyen, N., Giles, M., Peraire, J., 2016. An empirical interpolation and model-variance reduction method for computing statistical outputs of parametrized stochastic partial differential equations. SIAM/ASA Journal on Uncertainty Quantification 4 (1), 244–265.
[57] Vidal-Codina, F., Nguyen, N.-C., Giles, M. B., Peraire, J., 2015. A model and variance reduction method for computing statistical outputs of stochastic elliptic partial differential equations. Journal of Computational Physics 297, 700–720.
[58] Yasumoto, K., 2005. Electromagnetic theory and applications for photonic crystals. CRC press.
[59] Zepeda-Núnez, L., Demanet, L., 2016. The method of polarized traces for the 2D Helmholtz equation. Journal of Computational Physics 308, 347–388.